

Supplementary Figure Legends

Supplementary Figure 1.

A. Waterfall plot showing genes that are up- (blue) and down-regulated (orange) following Chi3l1 exposure. **B.** Scatterplot with a fitted linear regression line showing the relationship between Mesenchymal Gene-Expression Signature (MGES) gene enrichment and Chi3l1-treated gene enrichment. **C.** Western blot analysis using GSC2 lysates of phosphorylation of beta-catenin(s675), Akt(s473), and total CD44 in GSCs with small interfering RNA (siRNA) targeting negative control (scrambled siRNA) or CD44 and treated with or without Chi3l1 showing that knockdown of CD44 inhibits the Chi3l1 induced phosphorylation of Akt and beta-catenin. For knockdown of CD44 we used individual targeting siRNAs from Dharmacon (cat no: J-009999-06-0020).

Supplementary Figure 2.

A, C, E, G. Jaccard Raincloud plots show the stability of each cluster for GSC1 (A), GSC2 (C), GSC3 (E), and GSC4 (G). The boxplots with a half-size violin plot displays the distribution of the Jaccard indices before and after re-clustering across 100 subsamples. The dotted lines denote Jaccard indices cutoffs at 0.6 and 0.75 (a cluster is deemed stable when its mean Jaccard index is >0.80 and unstable <0.60). **B, D, F, H.** Uniform manifold approximation and projection (UMAP) of anchored GSCs colored by annotated stable clusters for each condition (Right).

Supplementary Figure 3.

A, Fragment tag density plots at the promoter sites with increased accessibility. **B,** Correlation plots of the fragment counts for each set of technical replicates. **C,** Expression of activated TFs in 44 GSCs (Data extracted from Mack et al. JEM 2019)

(4). **D**, Distribution of MAZ expression in NSC and GSC (n=8 in NSCs; n=44 in GSCs)
(Data extracted from (4).

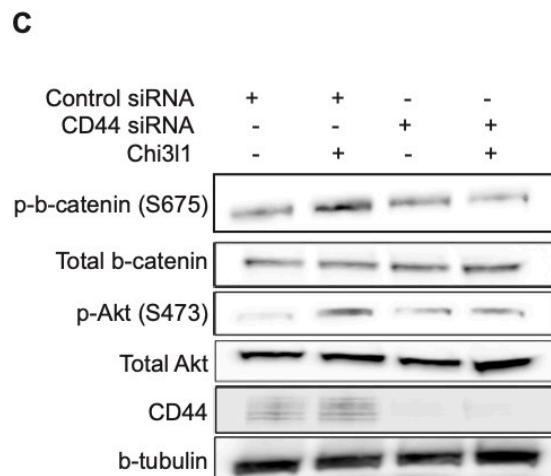
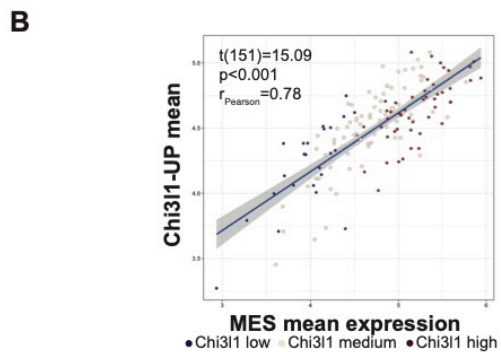
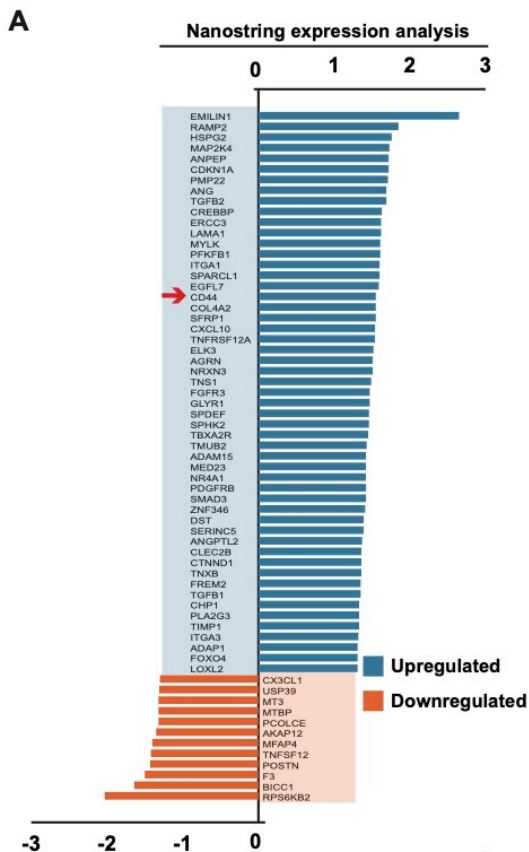
Supplementary Figure 4.

A, Recombinant human and mouse Chi3l1 protein of variable concentrations 250, 125, 62.5, 31.2, 15.6 and 7.8 (ng/ml) detected using purified Chi3l1 monoclonal antibody (1 µg/ml). **B**, Dose response curve determined the anti-Chi3l1 kd value is $\sim 1.1 \times 10^{-8}$. **C**, Determination of the limit of detection of the anti-CHI3L1 antibody with ELISA assay. Optical density plotting as a function of Chi3l1 concentration. **D**, Western blot showing inhibition of MAZ expression with a second siRNA different from the one reported in Figure 6. **E**, Tumor sphere formation assay with and without addition of Chi3l1 and with and without inhibition of MAZ with siRNAs. Inhibition of MAZ induces significant ($p < 0.01$) inhibition of tumor sphere formation. **F**, Limited dilution assay (LDA) for self-renewal and tumor sphere assay following inhibition of MAZ with siRNAs in the absence of Chi3l1. MAZ knockdown results in significant inhibition of self-renewal and tumor sphere formation.

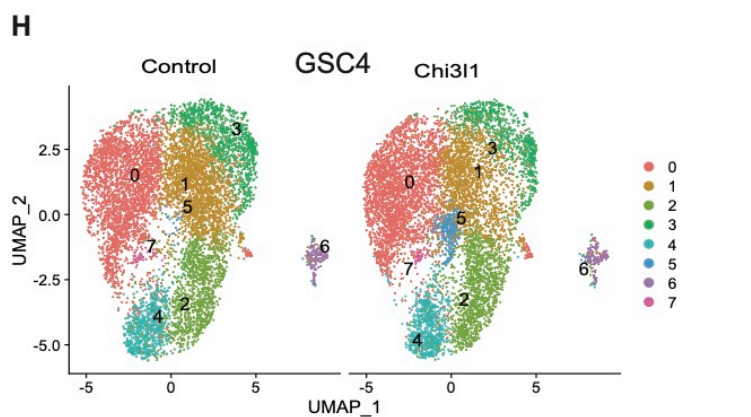
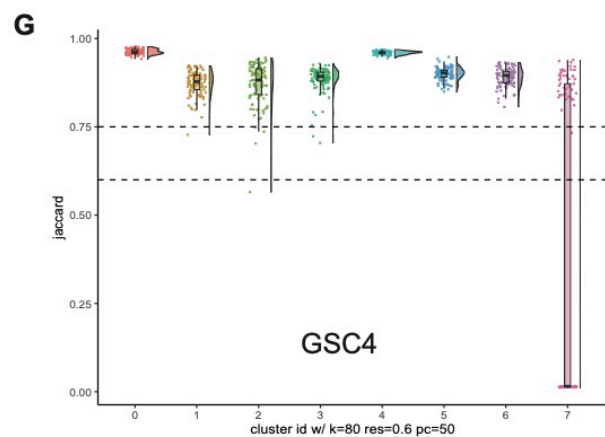
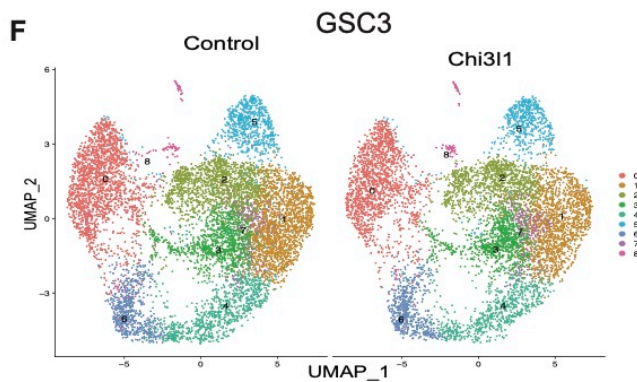
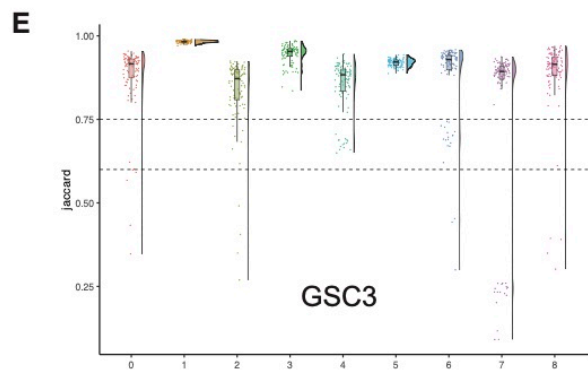
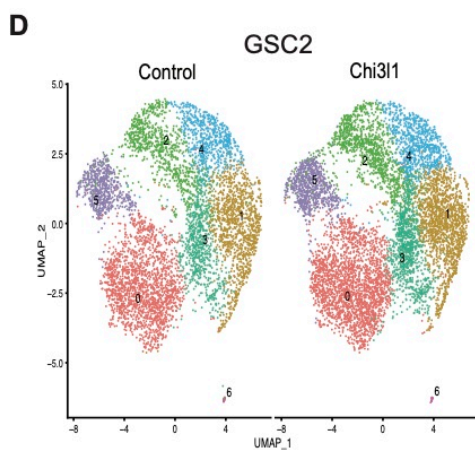
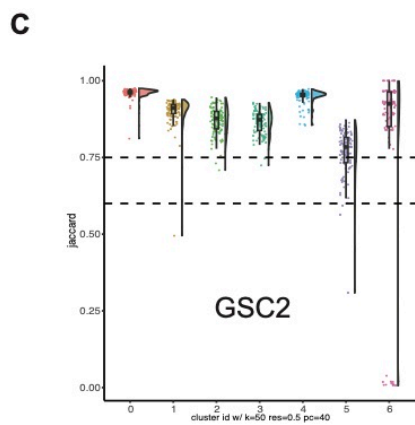
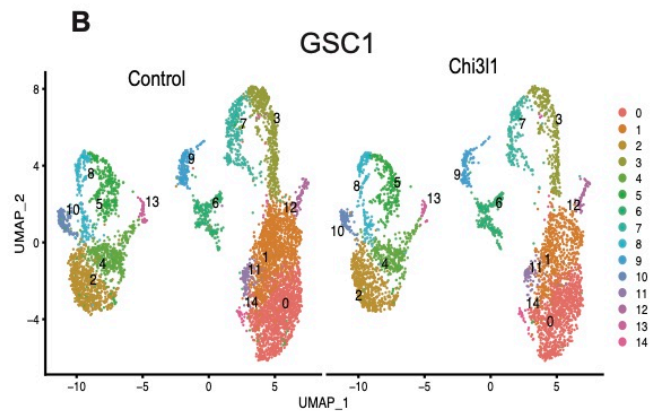
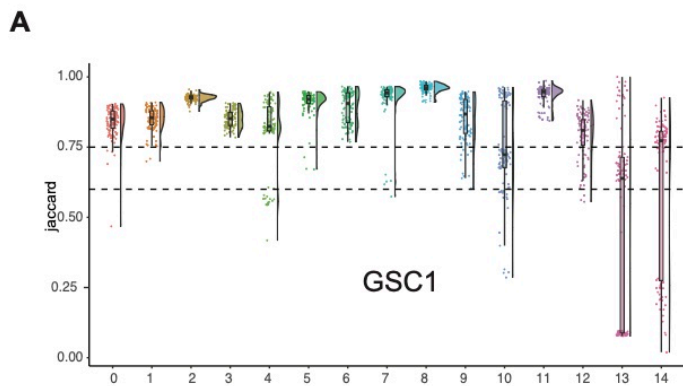
Supplementary Figure 5:

Uniform manifold approximation and projection (UMAP) of GSCs colored based on Verhaak's Proneural (PN) and Mesenchymal (MES) transcript expression.

Supplementary Figure 1

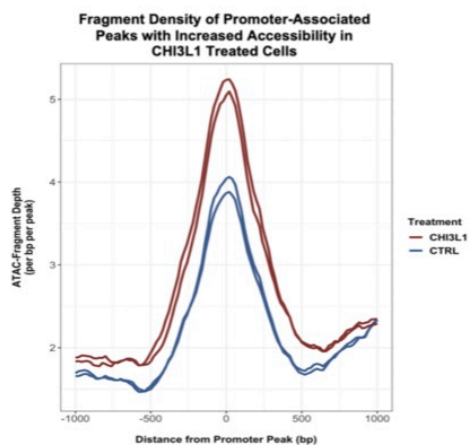


Supplementary Figure 2

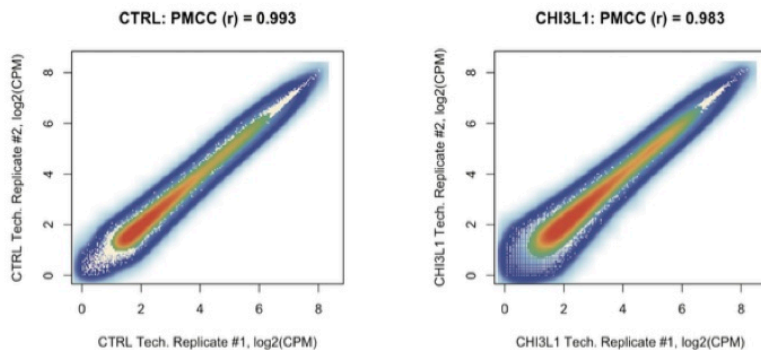


Supplementary Figure 3

A

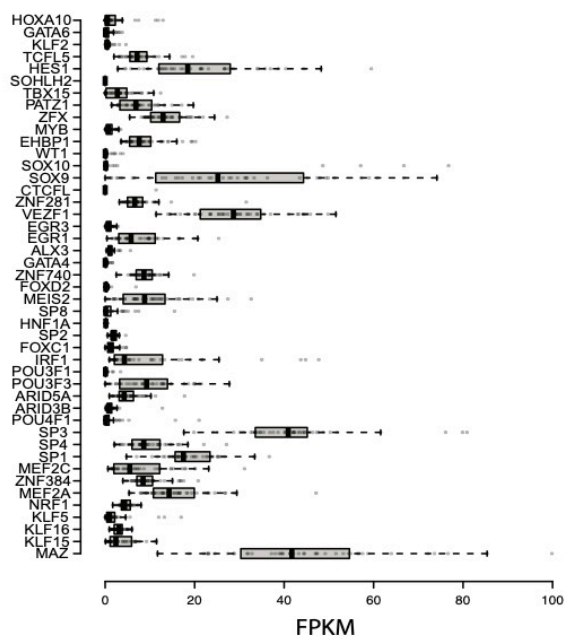


B

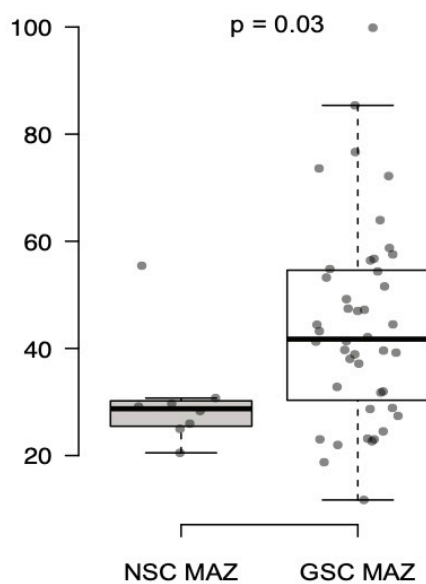


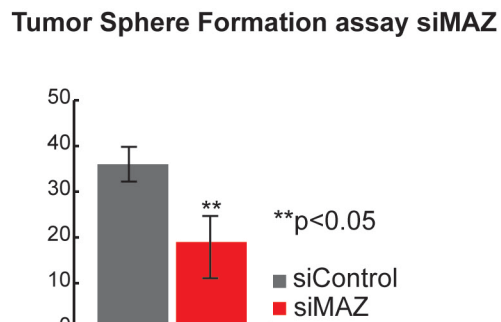
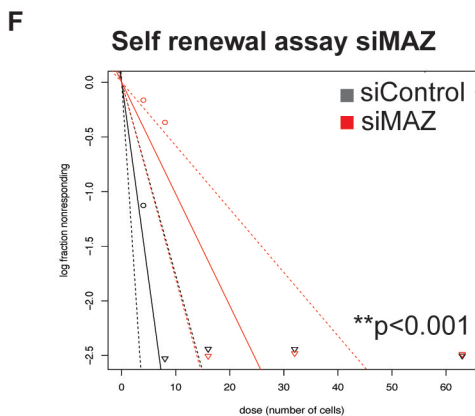
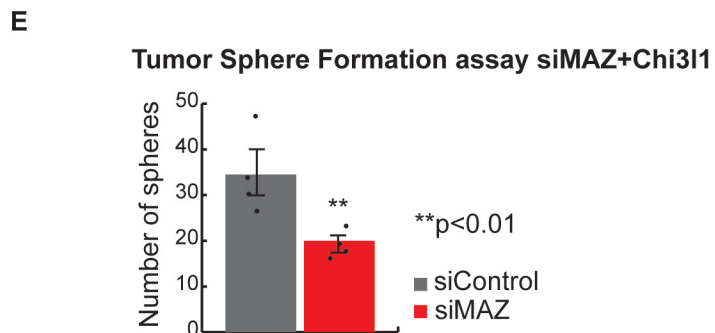
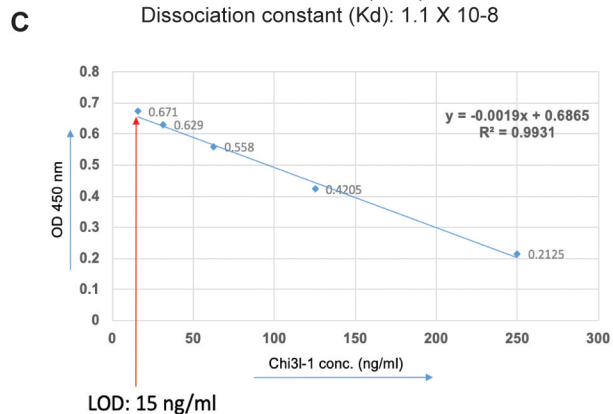
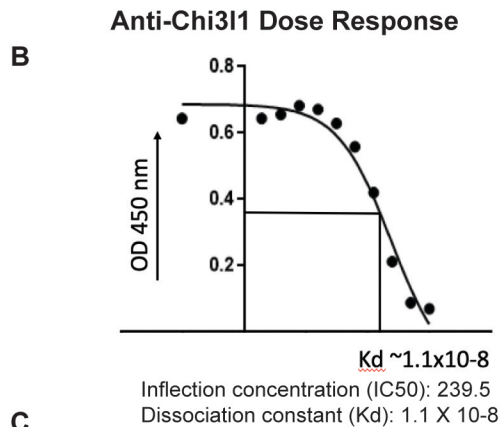
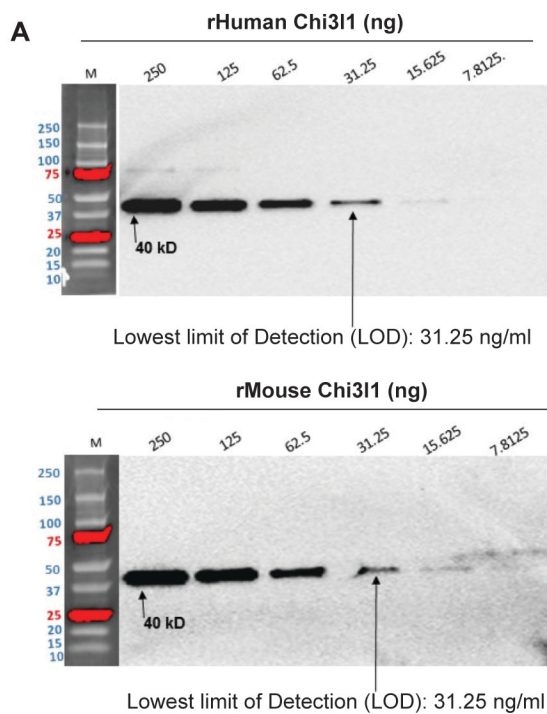
C

Expression of activated TFs in GSCs (n=44)



D





Supplementary Figure 5

